École Polytechnique Fédérale de Lausanne

Master's Thesis

Investigation into the Breakup of a Geostationary Satellite

Aubin Mercier
supervised by Stephan Hellmich

July 10, 2026

Abstract

This project investigates the fragmentation event of the decommissioned geostationary satellite Luch/Olymp that occurred on January 30, 2026. The event, recorded by the Swiss company s2aSystems, has no clear explanation, and the resulting debris cloud is unknown. After star detection and plate solving of the images, nine fragments are detected and their orbits are determined. Analyses using Gabbard diagrams and comparison to simulations using the NASA Standard Breakup Model are conducted. It is concluded that the fragmentation was likely a low-energy event, possibly caused by a battery failure.

Acknowledgements

I would like to express my sincere gratitude to everyone who contributed to the success of this project. First and foremost, I thank Stephan Hellmich from the EPFL Space Center for his guidance as my supervisor. His profound knowledge in space sustainability and astronomical images processing greatly enriched the quality of the work presented here.

I am also deeply appreciative of the company s2aSystems, and especially Roger Spinner, for making this work possible by sharing the images, as well as for his support and insightful feedback throughout the project.

I would also like to thank Thibault Kuntzer for providing valuable data and thoughtful feedback during the project.

Special thanks are extended to Jean-François Molinari, Guillaume Anciaux and Pavan Nanduri for their expertise in numerical modeling, especially in breakup model.

Lastly, I wish to thank the EPFL Space Center for their academic support, which was instrumental in bringing this work to fruition.

Contents

Abstract . . . 2
Acknowledgements . . . 3
Table of contents . . . 4
List of Figures . . . 5
List of Tables . . . 6

1 Introduction **7**
1.1 Context . . . 7
1.2 Objectives of the project . . . 7
1.3 Definitions and abbreviations . . . 8

2 Background & Theory **9**
2.1 Space Situational Awareness . . . 9
2.2 GEO Environment and debris persistence . . . 10
2.3 Orbital mechanics in GEO . . . 10
2.4 Kessler syndrome and collision cascading . . . 12
2.5 Satellite fragmentation . . . 12
2.6 Gabbard Diagrams . . . 14
2.7 NASA Standard breakup model . . . 15

3 Observational Data & Instrumentation **16**
3.1 Satellite data . . . 16
3.2 Telescope and sensor setup . . . 16
3.3 Dataset overview . . . 17
3.4 Event description . . . 17

4 Processing pipeline **19**
4.1 Image pre-processing . . . 19
4.2 Astrometric solution . . . 20
4.3 Fragment detection & tracklet creation . . . 21
4.4 Orbit determination . . . 23

5 Analysis **27**
5.1 Gabbard diagrams . . . 27
5.2 SBM application to Luch/Olymp . . . 28

6 Discussion **30**
6.1 Breakup cause hypotheses revisited . . . 30
6.2 Comparison with other GEO fragmentation events . . . 30
6.3 Limitations of the study . . . 31

7 Conclusion **32**
7.1 Summary of Achievements . . . 32
7.2 Future work . . . 32
7.3 Lessons learned . . . 32

References **33**

List of Figures

2.1 Objects in orbit. Source: ESA Space Environment Report 9
2.2 Central acceleration and perturbative accelerations as a function of the distance r of the satellite from the center of the Earth, shown on a log–log scale. Source: Handbook of Satellite Orbits: From Kepler to GPS 11
2.3 Event causes and their relative share for all past fragmentation event. Source: ESA Space Environment Report 13
2.4 Example of a Gabbard diagram. Source: Tan, Reynolds, Schamschula 14
3.1 Telkom 3, using the Ekspress-1000N bus. Source: Manufacturer Image 16
3.2 Frames of the event 18
4.1 Pipeline schematic 19
4.2 Outputs at various steps of pre-processing 20
4.3 Original image (left) and stacked image (right) 22
4.4 Stacked image (left) and segmentation result (right) 22
4.5 Tracklets 23
4.6 Residuals evolution for fragment 3 24
4.7 Orbits distances matrix. TLEs are sorted by their NORAD IDs. 26
5.1 Gabbard diagram for observed fragments 27
5.2 Gabbard diagram of modeled fragments with no changes in parameters 28
5.3 Gabbard diagram of the 9 largest modeled fragments 29
6.1 Gabbard diagram of Intelsat33E fragments 31

List of Tables

1.1 Acronyms . . . 8
3.1 Satellite characteristics . . . 16
3.2 Optical properties . . . 17
3.3 Frames recorded . . . 17
3.4 Timeline of the event . . . 17
4.1 `.xyls` content for image in Fig.4.2 . . . 19
4.2 Additional parameters for the solving . . . 20
4.3 Solution statistics for different input dataset . . . 21
4.4 State vectors of determined orbits . . . 25
4.5 Formal uncertainties for each orbits . . . 25
5.1 KS test for different b values . . . 29
6.1 Confirmed fragmentation events in the GEO region . . . 30

1 Introduction

1.1 Context

The orbital environment is facing a growing challenge due to the accumulation of space debris, a situation caused by the rising number of decommissioned satellites that remain in orbit for years or even longer. In high altitude regions like the Geostationary Orbit and its graveyard orbit, the lack of atmospheric drag means that an object can persist for thousands or even millions of years. Decommissioned satellites are large unmaneuverable targets that could cause unintended collisions. They can also carry internal energy sources that can lead to spontaneous explosions if not properly passivated. A fragmentation event creates a cloud of debris that is a threat to operational satellites.

The Luch/Olymp satellite, launched in 2014, was decommissioned and moved to the graveyard orbit in October 2025. s2aSystems, a Swiss SSA/SDA company, has been acquiring observational data of this satellite and recorded a sudden breakup on January 30, 2026. According to the initial reports, either a space debris impact or a passivation failure may have cause the fragmentation.

The breakup of a large satellite like Luch in such a sensitive orbital region creates a new population of unmanaged debris, with potential long term consequences for the GEO environment. Understanding the characteristics of this debris cloud, both in terms of the fragments that can be directly observed and the larger population that remains undetected, is essential to assess the actual threat it represents for operational satellites in the coming decades.

1.2 Objectives of the project

This thesis aims to investigate the Luch/Olymp breakup event in order to better understand its causes and consequences. The work covers three main aspects. First, a precise astrometric solution is determined for each observation image using field stars, allowing the fragments released from the parent body to be detected and tracked. Second, the orbits of the fragments with sufficient observational coverage are determined. Finally, an analysis of the results is done, including a comparison with a breakup model.

The remainder of this thesis is organized as follows. Chapter 2 presents the theoretical background necessary to understand the orbital environment, the causes of satellite fragmentation, and the tools used in this work. Chapter 3 describes the observational data, the instrumentation used to acquire it, and the event itself. Chapter 4 details the processing pipeline, from image pre-processing to astrometric solution, fragment detection and tracklet creation, and orbit determination. Chapter 5 presents the analysis, including the Gabbard diagrams, the application of the NASA Standard Breakup Model, and the comparison between the model predictions and the observed fragment population. Chapter 6 discusses the results in light of the different breakup hypotheses and compares the event with other documented GEO fragmentations. Chapter 7 concludes the thesis with a summary of the achievements, directions for future work, and lessons learned from the project.

AI tools were used to assist with portions of this report.

1.3 Definitions and abbreviations

Acronym	Definition
DEC	Declination
ESA	European Space Agency
GEO	Geostationary Orbit
GTO	Geosynchronous Transfer Orbit
ITU	International Telecommunication Union
LEO	Low-Earth orbit
NASA	National Aeronautics and Space Administration
RA	Right Ascension
SBM	NASA Standard Breakup Model
SDA	Space Domain Awareness
SNR	Signal-to-Noise Ratio
SRP	Solar Radiation Pressure
SSA	Space Situational Awareness
SSN	United States Space Surveillance Network
TLE	Two-Lines Element
WCS	World Coordinate System

Table 1.1: *Acronyms*

2 Background & Theory

This section presents the theoretical background necessary to understand the context and methodology of this work. It starts with an overview of Space Situational Awareness and the tools used to monitor the orbital environment, then describes the specificities of the geostationary orbit and the reasons why debris persistence is particularly concerning at this altitude. The orbital mechanics governing the long term evolution of debris at GEO altitude are then introduced, followed by a discussion of the Kessler syndrome and the risk of collision cascading. The chapter then reviews the causes and typology of satellite fragmentation events. Finally, two tools that will be used in this work are presented : the Gabbard diagram, which is used to visualize the fragment distribution resulting from a breakup, and the NASA Standard Breakup Model, which allows to estimate the fragment population.

2.1 Space Situational Awareness

Space Situational Awareness (SSA) refers to the knowledge and capacity to detect, track and characterize objects in orbit around the Earth. In practice, this means being able to know at any time where are the objects in orbit, what is their size, and how their trajectory will evolve. A related term, Space Domain Awareness (SDA), is sometimes preferred as it includes a broader scope, covering also the intent and behavior of space actors, not only the physical tracking of objects.

The need for SSA has grown significantly in the last decades, mainly because of the increasing number of objects in orbit. As of May 2026, about 44 870 objects (Fig.2.1) are regularly tracked by Space Surveillance Networks and maintained in their catalogue, and more than 1.2 million space debris object greater than 1cm are in orbit, according to the latest European Space Agency's (ESA) Space Environment Report [1]. Most of these objects are concentrated in Low Earth Orbit (LEO), but the Geostationary Orbit (GEO) is also a region of high interest because of its strategic and economic value.

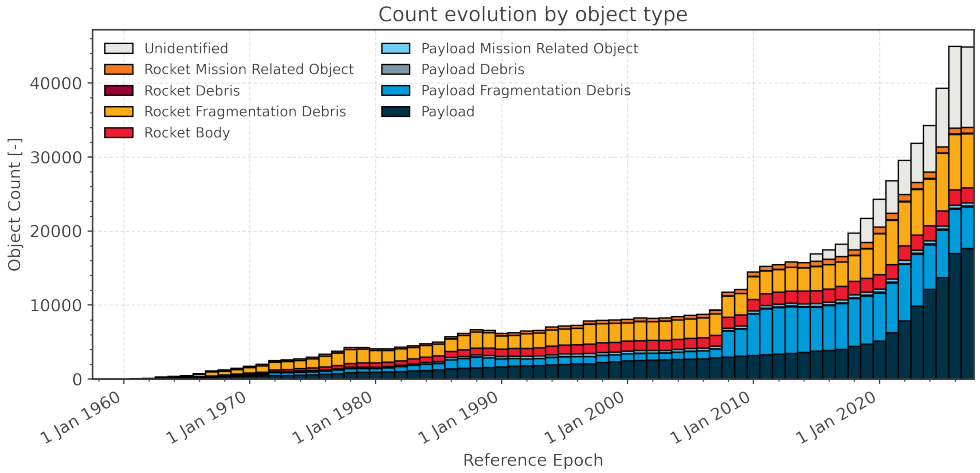

Figure 2.1: *Objects in orbit. Source: ESA Space Environment Report*

SSA relies on a combination of radar systems and optical telescopes. Radars are generally more effective for LEO objects, while optical sensors are preferred for high-altitude regions like GEO, where the objects are too far for most radar systems but can be observed by telescopes. The main actors in SSA are governments agencies, like the United States Space Surveillance Network (SSN), which maintains a public catalog of space objects, or ESA with the Space Debris Office. There are also an increasing number of private companies.

The data collected by SSA systems is used to compute Two-Line Elements (TLEs), which are a

standardized format to describe the orbit of an object at a given epoch. TLEs are widely used in the space community but their accuracy is limited, especially for objects in GEO where the orbital dynamics are more complex and the tracking cadence is lower than in LEO. For fragmentation events or close approach situations, the precision of TLEs is often not sufficient, and dedicated follow-up observations are required to properly assess the risk. This is especially true in GEO, where the lower tracking frequency makes it harder to maintain accurate orbital solutions for newly detected objects.

Among the orbital regions monitored by SSA systems, the Geostationary Orbit deserves particular attention due to its strategic value and the unique challenges it poses in terms of debris persistence.

2.2 GEO Environment and debris persistence

The Geostationary Orbit is a circular orbit located at an altitude of approximately 35,786 km above the equator. At this altitude, the orbital period of a satellite matches exactly the rotation period of the Earth, which means that from the ground, a geostationary satellite appears fixed in the sky. This property makes GEO extremely valuable for telecommunications, weather monitoring and broadcasting applications, as a single satellite can cover a large portion of the Earth surface continuously without requiring ground antennas to track it.

Because of this strategic value, the geostationary belt is a limited and heavily used resource. Satellites are assigned specific longitude slots by the International Telecommunication Union (ITU), and there is 573 active satellites in GEO as of January 2026 [2]. This concentration of high-value assets makes the orbital environment particularly sensitive to any event that could generate new debris.

From an orbital mechanics point of view, GEO is a relatively stable region. The main perturbation forces at this altitude are the solar radiation pressure, the lunisolar gravitational attraction, and the tesseral harmonics of the Earth gravity field. These forces cause slow drifts in longitude and inclination over time, but they are not strong enough to remove objects from the region. Unlike in LEO where atmospheric drag causes satellites to naturally re-enter the atmosphere within years or decades, there is no equivalent decay mechanism at GEO altitude. An object placed there will remain for thousands of years without active intervention.

For this reason, an international guideline has been established to mitigate the long-term contamination of the geostationary belt. At the end of their operational life, satellites are supposed to be moved into a so-called graveyard orbit, located approximately 200 to 300 km above GEO. This maneuver, called a disposal or re-orbiting maneuver, requires a small amount of remaining propellant and is intended to free the geostationary slot for future operators.

However, the graveyard orbit is not a perfect solution. Objects placed there are still in a region with no natural decay, and any fragmentation event produces debris that will remain in the vicinity of GEO for an extremely long time. As a result, the population of uncontrolled objects in and around GEO is slowly growing, increasing the long term risk for operational satellites.

To assess how this population evolves over time, it is necessary to understand the perturbation forces that govern the motion of uncontrolled objects at GEO altitude.

2.3 Orbital mechanics in GEO

Once a fragmentation event occurs, the resulting debris cloud does not stay concentrated around the breakup point. Each fragment follows its own orbit, and over time the cloud spreads along and around the original orbit due to the differences in orbital energy between fragments. Understanding how these orbits evolve over long time scales requires taking into account several perturbation forces that act on objects at GEO altitude.

One important perturbation at GEO is the non-uniform distribution of the Earth gravitational field (see Fig.2.2) [3], and in particular the tesseral harmonics, which cause objects to drift in longitude to-

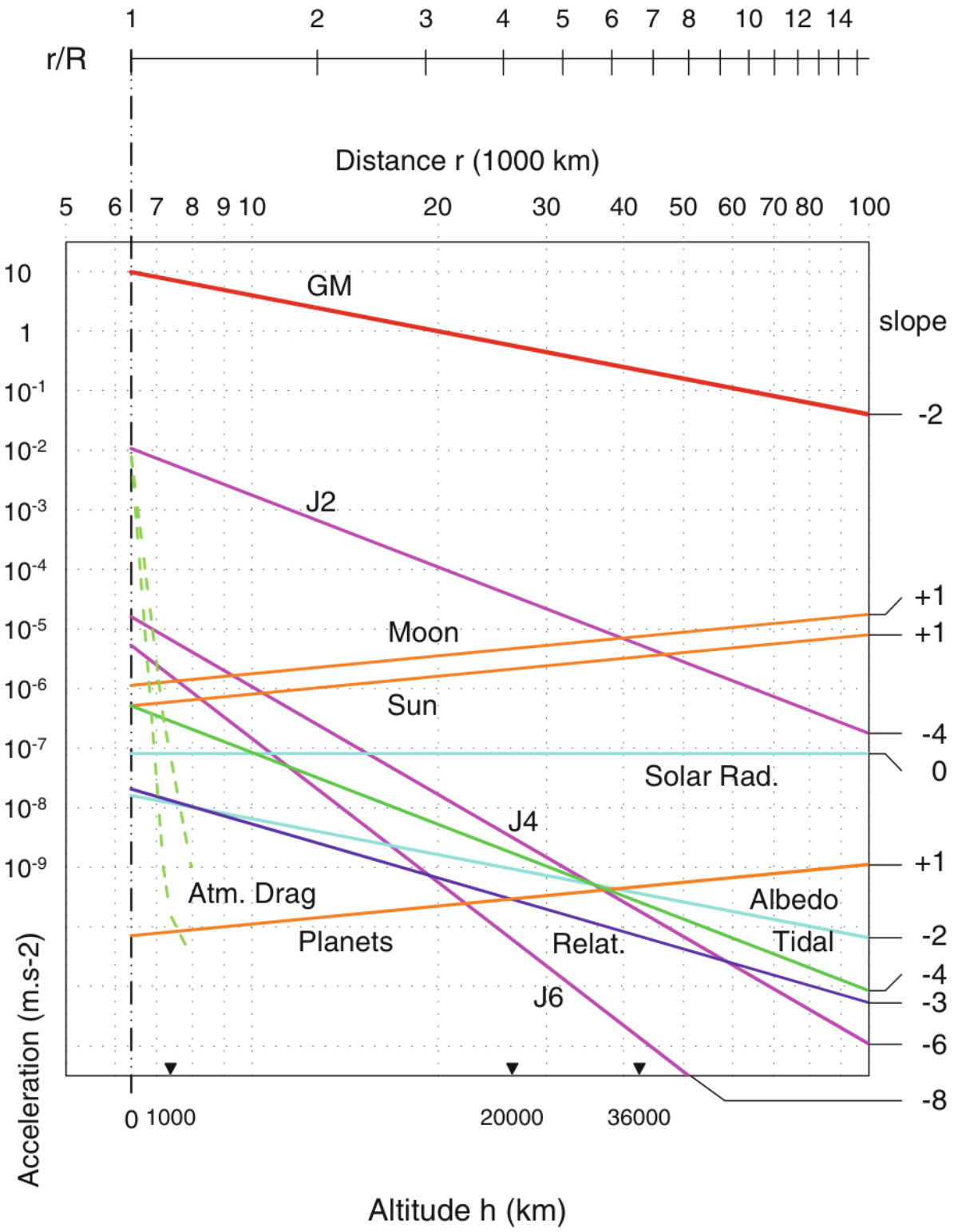

Figure 2.2: *Central acceleration and perturbative accelerations as a function of the distance r of the satellite from the center of the Earth, shown on a log–log scale. Source: Handbook of Satellite Orbits: From Kepler to GPS*

ward two stable equilibrium points located at approximately 76°E and 103°W. Uncontrolled objects in GEO will naturally librate around one of these points over periods of several years, which means that debris from a fragmentation event will not spread uniformly along the entire geostationary ring but will tend to concentrate in certain longitude regions over time.

The second important perturbation is the lunisolar gravitational attraction from the Moon and the Sun [3]. At GEO altitude this effect is non negligible and causes an increase in orbital inclination over time for uncontrolled objects. Operational satellites counteract this effect with regular station keeping maneuvers, but debris fragments have no such capability and will see their inclination grow over decades, which further modifies the geometry of potential conjunctions with operational satellites.

The third perturbation to consider is the solar radiation pressure (SRP) [3], which is caused by the momentum transfer of photons from the Sun onto the satellite surface. The magnitude of this effect depends on the area-to-mass ratio of the object, which means that small and lightweight fragments with a large surface area are affected much more strongly than compact and heavy ones. SRP causes oscillations in eccentricity and inclination over time, and for high area-to-mass ratio fragments the effect can be significant enough to bring the perigee of the orbit down toward the operational GEO belt, which has direct implications for the collision risk with active satellites.

In the most extreme scenario, this growing conjunction risk can lead to a self sustaining cascade of collisions, a concept known as the Kessler syndrome.

2.4 Kessler syndrome and collision cascading

The Kessler syndrome, first described in 1978 by Donald Kessler and Burton Cour-Palais [4], refers to a scenario where the density of objects in orbit becomes high enough that collisions between them generate new debris, which in turn increases the probability of further collisions, creating a self-sustaining cascade. Once this threshold is reached, the process becomes independent of any new launches and the affected orbital region could become unusable for future generations.

The concept is mainly applied in the context of Low Earth Orbit, where the debris population is the densest and where the consequences of a cascade would be the most immediate. However, the same logic applies to GEO, with some important differences. In LEO, fragments from a collision will eventually re-enter the atmosphere due to drag, which limits the lifetime of the debris and gives the environment a natural cleaning mechanism. In GEO, as discussed in section 2.2, there is no such mechanism, meaning that every fragment produced by a collision stays in the region for thousands of years.

The risk of collision cascading in GEO is today considered lower than in some LEO shells, mainly because the objects are more spread out along the geostationary ring. However, the situation is slowly getting worse as the number of uncontrolled objects increases. A fragmentation event that produces a cloud of new debris in GEO or in the graveyard region directly contributes to this trend, and the long term assessment of the resulting debris cloud is an important task.

To properly characterize a debris cloud, it is first necessary to understand what caused the fragmentation event, as the cause directly influences the properties of the resulting fragment population.

2.5 Satellite fragmentation

Fragmentation events in orbit can be caused by several mechanisms, and understanding the cause is important because it directly affects the characteristics of the resulting debris cloud, in particular the number of fragments, their size distribution, and the velocity they are ejected with. It is also useful to distinguish between total fragmentation, where the parent body is completely destroyed and no significant remnant survives, and partial fragmentation, where the main body remains mostly intact but releases a number of fragments. The latter is actually more common in practice, and is

the typical outcome of an on-board explosion or a low energy impact.

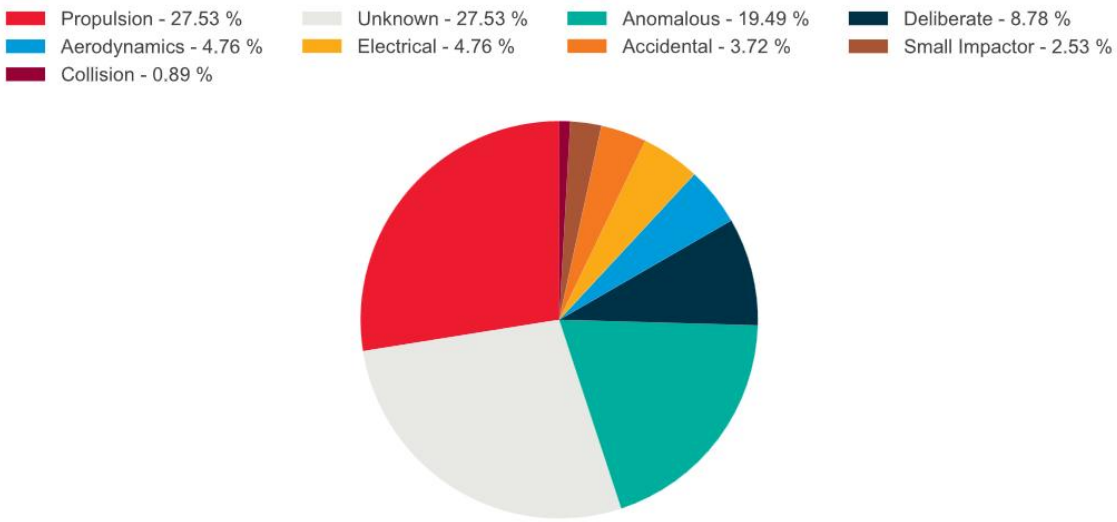

Figure 2.3: *Event causes and their relative share for all past fragmentation event. Source: ESA Space Environment Report*

The main causes of fragmentation (see Fig.2.3) can be grouped as follows :

Passivation failures At the end of their operational life, satellites carry residual energy sources such as pressurized propellant tanks and batteries. If these are not properly neutralized, they can explode spontaneously years or even decades after decommissioning. This type of event is actually responsible for the majority of documented fragmentation events in orbit according to the ESA Space Debris Environment Report [1]. Battery explosions and propellant tank ruptures typically produce a relatively symmetric velocity distribution in the resulting fragment cloud, which is a useful diagnostic when trying to determine the cause of an observed breakup. One representative example is the unexpected fragmentation of NOAA-16 in November 2015. The retired weather satellite broke apart after nearly two years of inactivity, most likely due to the release of stored energy from its batteries. The event generated more than 200 trackable debris objects, illustrating how inadequate passivation can continue to pose a hazard long after a spacecraft has ceased operations.

Hypervelocity impacts A collision between two orbital objects at very high relative velocity, whether it involves two intact satellites, a satellite and a rocket body, or a satellite and a small debris fragment, can severely damage or completely destroy the target. At orbital velocities, even a small object carries enough kinetic energy to severely damage or completely shatter a larger one. One of the most documented example of a collision between two objects is the impact between Iridium 33 and Cosmos 2251 in February 2009, which produced more than 2000 trackable fragments in LEO and is considered the first accidental hypervelocity collision between two intact satellites [5]. Whether the result is a total or partial fragmentation depends mainly on the mass ratio between the two objects and on their relative velocity at the moment of impact.

Voluntary destruction A satellite can also be intentionally destroyed, either through a dedicated anti-satellite weapon test or through a controlled deorbit that goes wrong. The most significant example in terms of debris generation is the Chinese ASAT test of January 2007, where the Fengyun-1C weather satellite in LEO was deliberately destroyed, creating more than 3000 trackable fragments and significantly worsening the debris environment in that orbital region [6]. While voluntary destructions in GEO are rare, the legal and political context around ASAT testing remains relevant to the broader debris problem.

Once a fragmentation event has occurred, a practical tool to visualize and analyze the resulting debris cloud is the Gabbard diagram, which is introduced in the following section.

2.6 Gabbard Diagrams

A Gabbard diagram is a graphical tool commonly used in orbital debris analysis to visualize the distribution of fragments resulting from a fragmentation event. It was introduced by Joseph Gabbard at NASA in the late 1970s as a practical way to analyze debris clouds from a large number of fragments without having to examine each orbit individually. A detailed discussion of the theoretical basis can be found in Tan, Reynolds and Schamschula who applied it to the fragmentation of the NOAA-16 satellite [7].

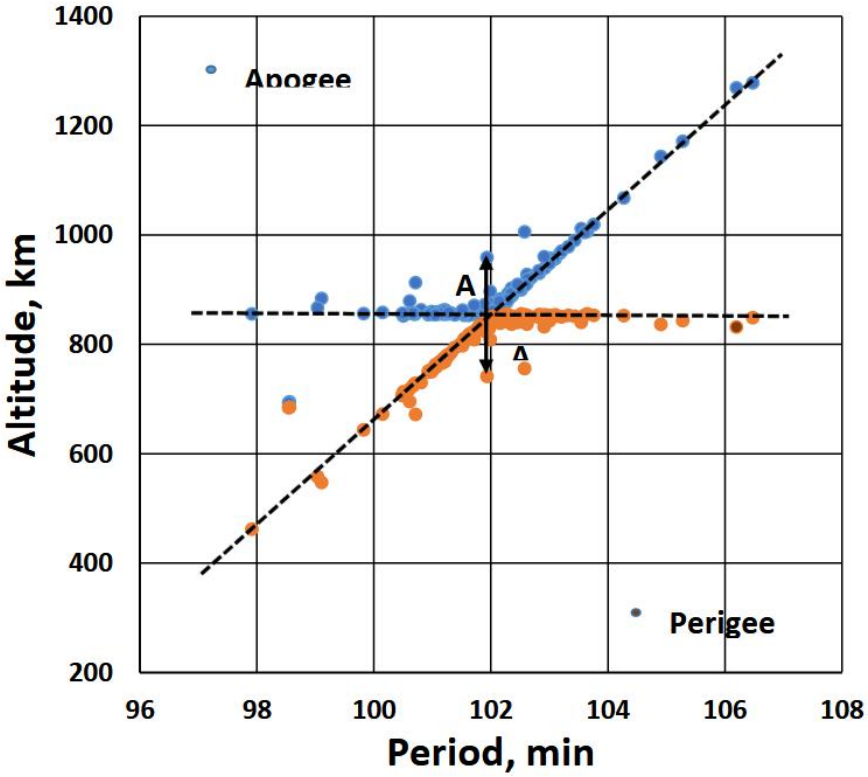

Figure 2.4: *Example of a Gabbard diagram. Source: Tan, Reynolds, Schamschula*

In a Gabbard diagram, each fragment is represented by two points, one for the apogee and one for the perigee of its orbit (respectively blue and orange in Fig.2.4). The horizontal axis shows the orbital period of the fragment, and the vertical axis shows its apogee and perigee altitudes. This produces two curves, one for apogees and one for perigees, that together form a characteristic shape often described as a butterfly or a bowtie. The fragment corresponding to the original orbit of the parent body sits at the center of this shape, and the spread of the two curves around it reflects the velocity increment, or Δv, that was imparted to each fragment at the moment of the breakup.

The shape and symmetry of the Gabbard diagram can give useful information about the nature of the fragmentation event. A symmetric diagram, where the apogee and perigee curves are roughly mirror images of each other, is consistent with an explosion where fragments are ejected in all directions with similar velocities. An asymmetric diagram, on the other hand, can indicate a directional event such as an impact, where the impactor imparts a preferential velocity in a specific direction.

While the Gabbard diagram gives a visual picture of the trackable fragment population, it says nothing about the much larger number of fragments that are too small to be detected. This is where breakup models become necessary.

2.7 NASA Standard breakup model

When a fragmentation event occurs in orbit, it is generally not possible to detect and track all the fragments that are produced. Ground based sensors have a limited sensitivity, and a large fraction of the debris cloud, in particular the smallest fragments, remains invisible to current tracking systems. To estimate the total population of fragments including the untracked ones, breakup models have been developed. They can predict the characteristics of a debris cloud from a set of input parameters describing the event.

The most widely used of these models is the NASA Standard Breakup Model (SBM), originally developed in the 1990s and later updated by Johnson et al. in 2001 [8]. The model takes as input the mass of the parent object, the characteristic length and the type of event, either an explosion or a collision, and in the case of a collision also the mass and velocity of the impactor. From these inputs it generates a statistical distribution of fragments described by three parameters : the characteristic length of the fragment, its area-to-mass ratio, and the velocity increment it received at the moment of the breakup.

The fragment size distribution follows a power law, meaning that the number of fragments increases rapidly as their size decreases. For a typical explosion event, the model predicts tens of thousands of fragments larger than 1 cm, of which only a few hundred may be large enough to be tracked by ground based observation systems. This large discrepancy between the tracked and the total population is one of the main motivations for using a breakup model in debris risk assessments.

The area-to-mass ratio distribution predicted by the SBM is particularly important for long term orbit propagation, because as discussed in section 2.3, the effect of solar radiation pressure on a fragment depends directly on this parameter. Fragments with a high area-to-mass ratio, such as thin sheets of insulation material or solar panel fragments, will have their orbits perturbed much more strongly than compact and dense fragments, leading to a much faster divergence of their trajectories over time.

The ejection velocity distribution describes how much Δv each fragment received relative to the parent body at the moment of the breakup. For an explosion event the distribution is roughly isotropic, meaning fragments are ejected in all directions with similar probabilities, while for a collision the distribution is more directional, reflecting the geometry of the impact. The typical ejection velocities predicted by the SBM for an explosion are of the order of a few tens to a few hundreds of meters per second, which at GEO altitude is enough to create a significant spread in orbital energy and therefore in the resulting orbital periods of the fragments.

It is worth noting that the NASA SBM was developed and calibrated primarily on fragmentation events observed in LEO, where the majority of documented breakups have occurred. Its applicability to GEO events, where the orbital dynamics are different and where observational data is more limited, is therefore not guaranteed. The velocity distributions and size distributions predicted by the model may not perfectly reflect the reality of a GEO fragmentation, and this is something to keep in mind when interpreting results obtained with the model in a high altitude context.

3 Observational Data & Instrumentation

This section presents the data available for this study. First, data on the satellite are summarized, followed by the description of the imaging setup and the acquired images. Finally the event is described.

3.1 Satellite data

The satellite, known as Luch, Olimp or Olymp-K, is a Russian GEO satellite of the Russian Ministry of Defence and Federal Security Service. Due to its military purposes, little information is known about its characteristics and mission. It was launched on September 28, 2014 from the Baikonur Cosmodrome, and placed into geosynchronous transfer orbit by the launcher. It performed multiple maneuvers and came within close proximity of other satellites in the GEO belt. Olymp-K was decommissioned and moved to a graveyard orbit in October 2025. A fragmentation occurred on January 30, 2026, the event that is the subject of this thesis.

Two different datasheets seems to coexist on the internet, shown in Table 3.1. The propulsion is probably an electric Hall-effect thruster with Xenon and a hydrazine thruster. The batteries of the Express-1000 bus are lithium-ion batteries (LIGP-50) by PAO Saturn.

	From GCAT [9]	From Gunther's space [10]
Bus	Ekspress-2000	Ekspress-1000
Dry Mass [kg]	1800	Unknown
Wet Mass [kg]	1930	3000
Size [m]	6.6x4.1x16	Unknown

Table 3.1: *Satellite characteristics*

In this project, the satellite is considered to have a wet mass of 3000kg and a dry mass of 2400kg.

Figure 3.1: *Telkom 3, using the Ekspress-1000N bus. Source: Manufacturer Image*

3.2 Telescope and sensor setup

The observing setup is composed of a RASA 36 telescope and a QHY600M camera. The optical properties are shown in Table 3.2. The tracking is set on the satellite using its TLE. This allows the satellite to be sharp at the cost of elongated stars.

Focal length	790mm
Aperture	355.6mm
Focal ratio	f/2.2
Pixel area	9576 x 6388
Pixel size	3.76 µm x 3.76 µm
Sensor size	Full frame (36mm x 24 mm)
Pixel field of view	0.98" x 0.98"
Frame field of view	156.4' x 104.3' (2.61°x 1.74°)

Table 3.2: *Optical properties*

3.3 Dataset overview

We will now go deeper into the dataset, presenting why it was acquired and its composition.

The satellite had an unusual behavior: despite being decommissioned, it maintained its attitude and was stable (its brightness was constant, which means it was not tumbling). The company s2aSystems therefore decided to monitor it. By chance, the fragmentation happened during the observation period, providing invaluable data about the event.

All acquired images and their characteristics are summarized in Table 3.3. The time is UTC on the day of January 30, 2026. The data can be separated into two categories, the short exposures, regrouping all the 1 second exposure images, and the long exposures, regrouping all the images with an exposure between 10 and 30 seconds. During this project, mostly the short exposures are used.

First frame time	Last frame time	Exposure time	Size	Binning	Number of frames
6h06:37	8h21:58	1s	640x480	-	8119
8h23:11	8h23:11	10s	9576x6388	-	1
8h23:23	8h23:45	20s	9576x6388	-	2
8h24:51	8h35:51	30s	9576x6388	-	22
8h37:09	8h38:56	20s	9576x6388	-	6
8h41:52	9h18:59	20s	4788x3194	2	125

Table 3.3: *Frames recorded*

3.4 Event description

Some information can be extracted by looking at the succession of images. The timeline of the event is presented in Table 3.4. There are at least 9 events with expulsion of matter as fragments or a cloud of gasses.

Time	Event
6h09:04	Gas and fragments release
6h14:15	Gas and probably fragments release
6h16:28	Small gas release
6h20:33	Gas release
6h22:09	Small gas release
6h23:01	Explosion, gas release
6h36:34	Big gas release
6h44:16	Big gas release
6h45:48	Gas release

Table 3.4: *Timeline of the event*

Some frames are shown in chronological order from left to right and top to bottom in Figure 3.2. The satellite is in the center of the image.

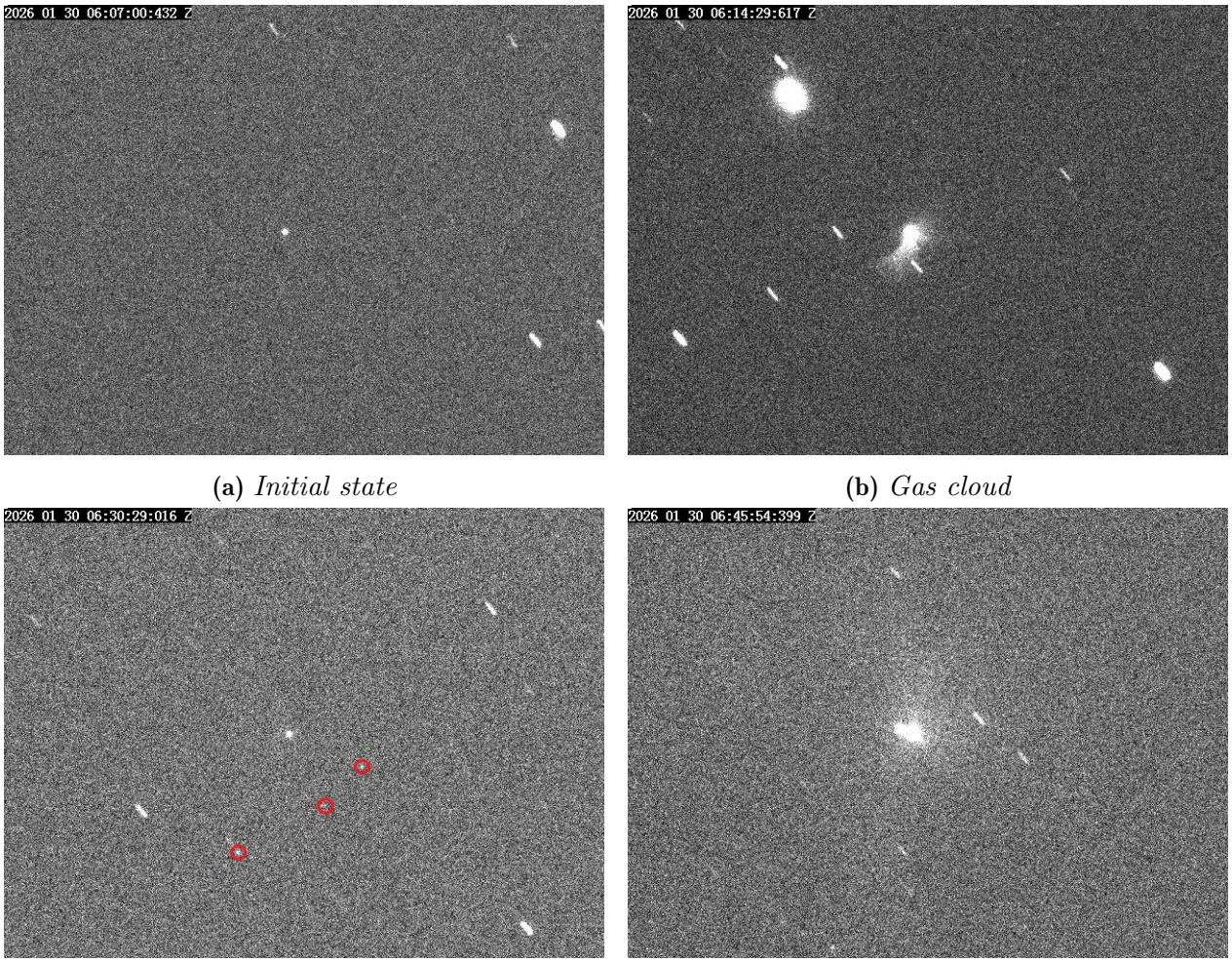

(a) *Initial state*

(b) *Gas cloud*

(c) *Fragments*

(d) *Gas cloud*

Figure 3.2: *Frames of the event*

4 Processing pipeline

The following section will describe the complete processing pipeline of the short exposure images, from raw images to orbit data. First the images are preprocessed to extract data for the plate solving which is the next step. Then a selection of images are stacked to extract the fragments and build tracklets. The coordinates of these tracklets are converted from pixel coordinates to sky coordinates, and finally the orbits are determined (see Fig.4.1).

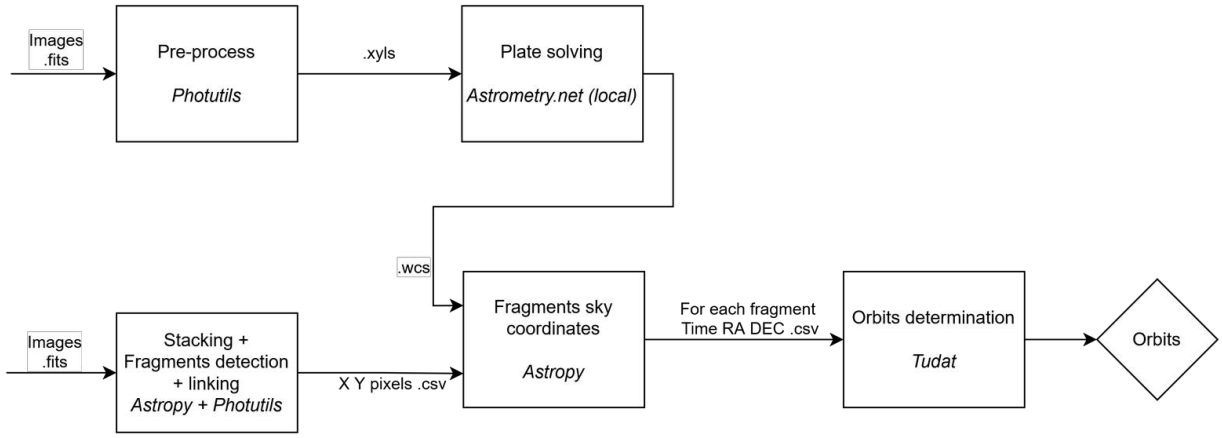

Figure 4.1: *Pipeline schematic*

4.1 Image pre-processing

During this first step, the raw `.fits` files undergo preprocessing, and a list of all detected objects is generated in an `.xyls` file. This is done using Astropy [11, 12, 13] and Photutils [14]. A mask is created to remove the timestamp and the central source, which corresponds to the parent object, to prevent them from skewing the analysis. The background is then calculated as the median of the image and subtracted. Finally, object detection is performed. It is done by image segmentation, a process that labels pixels in the image that belong to the same source (see Fig.4.2). Thanks to Photutils, several information can be retrieved about these segments, such as centroid position or shape properties. All pixel positions (x, y) are written in a `.xyls` file, which is a special kind of `.fits` file containing only 2 columns (X and Y) for position information (see Table 4.1).

This procedure works well for the short exposure images, where there are fewer and less elongated stars, but has inconsistent results on the long exposure images (multiple segment for a single star for example). This issue has not been solved for this project, so only the short exposure images will be used later.

X	Y
438.68647040886395	99.21992848237996
366.55890367043077	113.83098702527595
494.2513764643721	140.98683802629526
298.91760428209926	241.34232538381778
109.99249576357458	380.0580953616549
401.6281779333521	408.1439055729371
392.1269533793613	437.1885986369839

Table 4.1: *`.xyls` content for image in Fig.4.2*

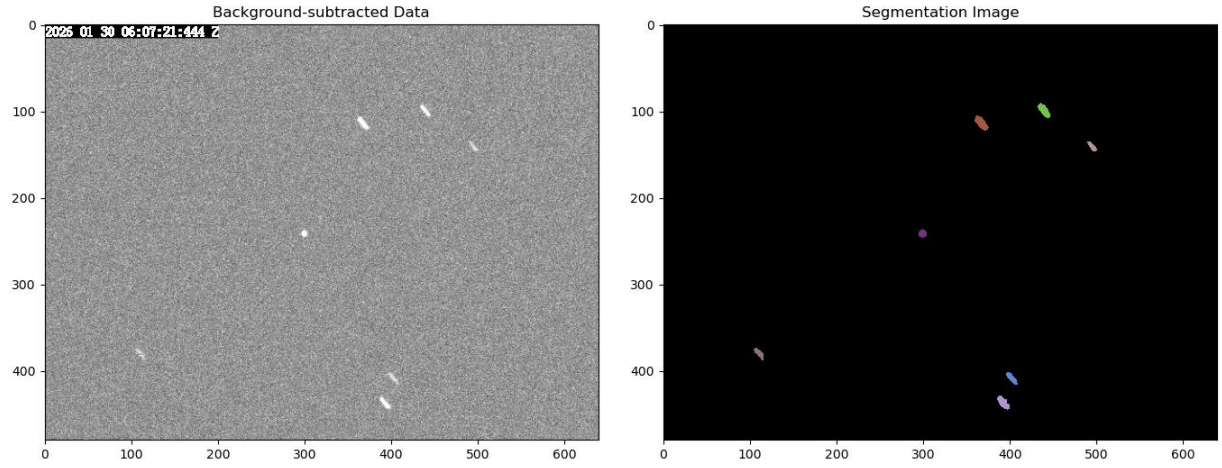

Figure 4.2: *Outputs at various steps of pre-processing*

4.2 Astrometric solution

In this step, the precise pointing and orientation of the image is determined from the `.xyls` file. This process is called plate solving. The output is a World Coordinate System (WCS) solution, which provides a mapping between the pixel coordinates of the image and the corresponding celestial coordinates on the sky.

This is done using the open source software Astrometry.net [15]. It matches the pattern of detected sources in the image against a reference star catalog, in this case a combination of the Tycho-2 and Gaïa-DR2 catalogs. If a match is found, it returns several files, most importantly a `.wcs` file containing the solution.

The plate solving is performed independently for each image. In addition to the `.xyls` file, some parameters (see Table 4.2) are given to the solver to limit the possible solutions. An approximate right ascension and declination is known from the acquisition setup and used as hint for the solver. The scale, which is the pixel field of view, is known from the optical path (see Table 3.2). The width and height are mandatory parameters when giving `.xyls` file as input and are the pixel size of the image.

Parameter	Value
Right Ascension	Read in the `.xyls` header
Declination	Read in the `.xyls` header
Radius	2.0°
Scale low	0.9"
Scale high	1.05"
Width	Read in the `.xyls` header
Height	Read in the `.xyls` header

Table 4.2: *Additional parameters for the solving*

Once a solution is found, one can assess its accuracy by computing the RMS error between the measured positions in the `.xyls` file to the real positions given in the `.corr` file, another output of astrometry.net.

To maximize both the number of solved images and the astrometric precision, two sets of preprocessed data were used as input to astrometry.net, differing only in the detection threshold applied during source extraction. Set 1 uses a high threshold, keeping only bright and well localized sources, which results in fewer detections but more precise positions. Set 2 uses a lower threshold to maxi-

mize the number of detected sources and including fainter ones, at the cost of and potentially less well localized objects. The two sets are then combined into a final dataset (set 1+2) using the following strategy : for each image, the `.xyls` file from set 1 is used if astrometry.net successfully found a WCS solution from it, and the `.xyls` file from set 2 is used otherwise. This way, images that are well covered by bright stars benefit from the higher precision of set 1, while images where set 1 failed to produce a solution are recovered using set 2. The statistics for each set are summarized in Table 4.3. The pixel scale of the instrument is approximately 0.98 arcseconds per pixel, so the RMS errors reported in pixels are roughly equivalent in arcseconds. Set 1+2 achieves the best overall performance, combining a high number of solved images and a maximum gap between two solved images of 88s, with a median RMS error of 0.57 pixels, and is therefore used for all subsequent steps.

Set	1	2	1+2
Number of images solved	3509	6216	6227
RMS Error at Median [pix]	0.41	0.90	0.57
Minimum RMS Error [pix]	0.01	0.07	0.01
Maximum RMS Error [pix]	2.37	3.11	2.38
RMS Error Standard Deviation [pix]	0.27	0.39	0.38
RMS Error at 95th percentile [pix]	0.98	1.63	1.38
Max gap [s]	389	88	88

Table 4.3: *Solution statistics for different input dataset*

4.3 Fragment detection & tracklet creation

This last step before orbit determination describes the detection of fragments in the images and the construction of tracklets, which are sequences of astrometric positions of the same object across multiple images. The output is a list of time and positions in sky coordinates (Right Ascension RA, Declination DEC).

The main challenge of this step is that the images contain a large number of sources, most of which are background stars, and the fragments must be identified and separated from this background population before they can be linked across images. An additional difficulty comes from the fact that some fragments may only be visible in a subset of images, either because they are too faint to be detected consistently or because they move out of the field of view, which makes the linking step more complex.

The approach chosen is to stack images. This allow to increase the signal to noise ratio (SNR) of the fragments (because they are at the same place at the time-scale considered), while removing the stars (because they are moving). The best result was obtained by median stacking 20 images before and 20 images after the reference image. The result is shown in Figure 4.3.

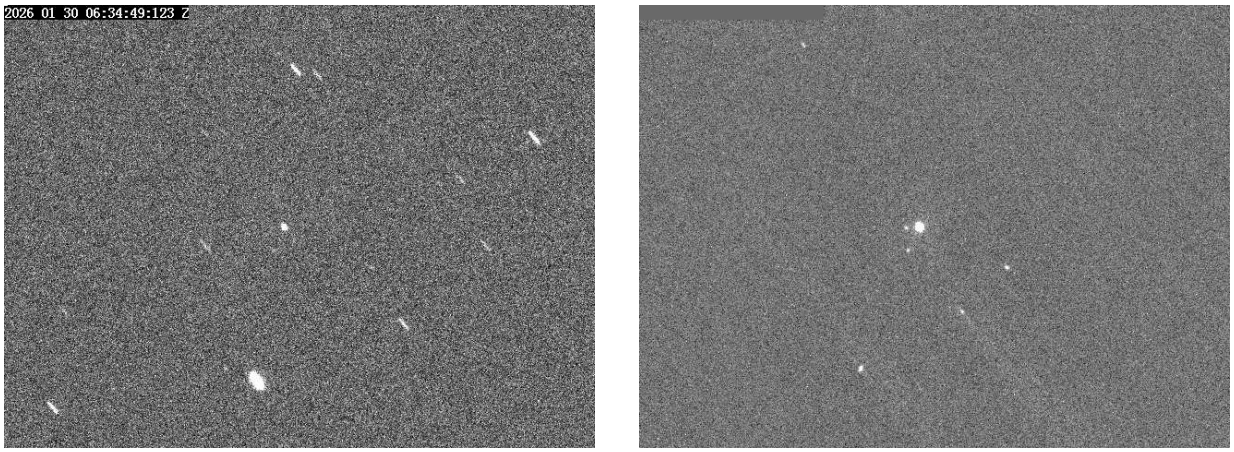

Figure 4.3: *Original image (left) and stacked image (right)*

Segmentation is then performed on the stacked image to detect fragment and retrieve their position, exactly the same as for star detection during the preprocessing step (see Fig.4.4). This outputs a list of positions of potential fragments. This list is compared to the objects known from previous images and fragments are linked using a greedy nearest-neighbour strategy based on Euclidean distance. If the new detection is close enough to a known object, it is appended to the tracklet, else a new one is created.

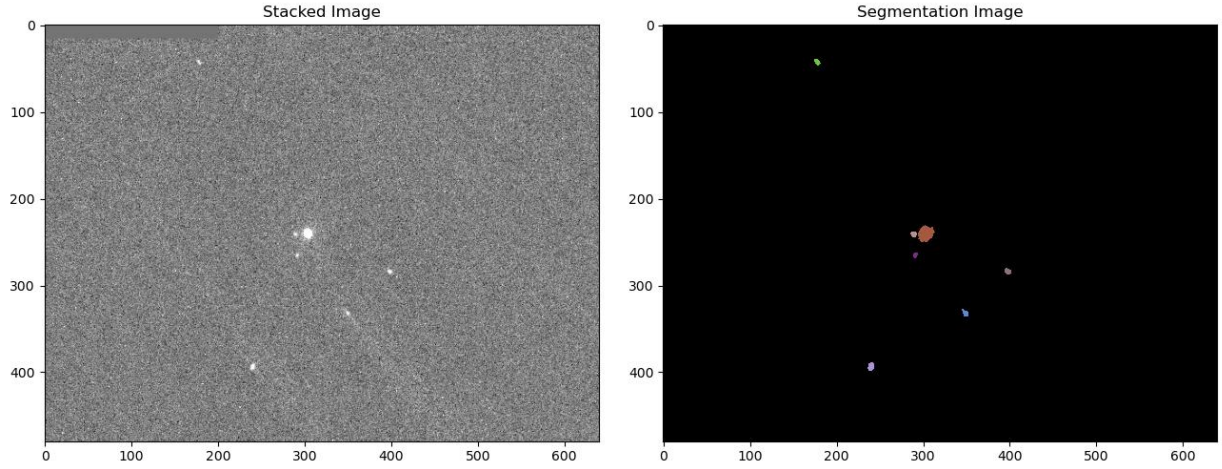

Figure 4.4: *Stacked image (left) and segmentation result (right)*

This process is done for a subset of images, roughly one reference image every 20 seconds (the image must have a WCS solution so it cannot be exactly every 20s), meaning the midpoints of two consecutive stacks are separated by roughly 20 seconds. Thanks to the stacking, the information of almost all the images is still used. Once the automated linking is done, some refinement needs to be done manually as sometimes, a new tracklet is created for an already existing object, or some tracklets are false detection. Finally, the list of pixel coordinates can be transformed in sky coordinates using the WCS obtained with astrometry.net.

Following this procedure, nine fragments were detected. Their tracklets in pixel coordinates are shown in Figure 4.5.

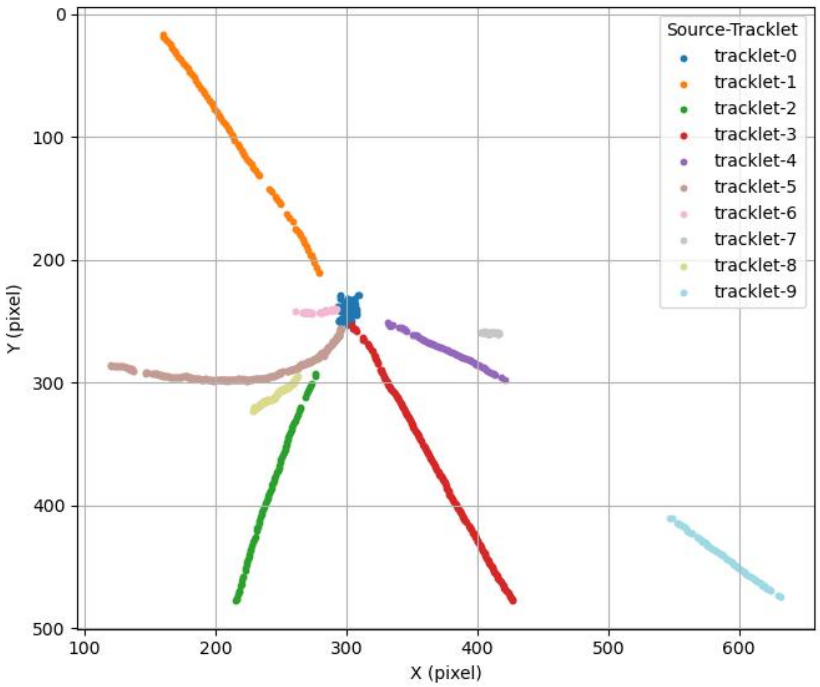

Figure 4.5: *Tracklets*

4.4 Orbit determination

The orbit determination step takes the data of each tracklet as input, and returns orbital data for the corresponding fragment.

4.4.1 Orbit determination framework: Tudat

Tudat, which stands for TU Delft Astrodynamics Toolbox, is an open source astrodynamics software framework developed at Delft University of Technology [16]. It is written in C++ with a Python interface and provides a wide range of tools for space mission analysis, orbit determination and propagation. The framework is modular, meaning that the user can assemble a simulation environment by selecting the relevant force models, integrators and estimation settings depending on the application.

For orbit determination, Tudat implements a batch least squares estimator that allows to fit a set of observations to a dynamical model and retrieve the best estimate of the initial state along with its covariance. For orbit propagation, Tudat supports a variety of force models including high degree gravity fields, atmospheric drag, solar radiation pressure, and third body gravitational attraction from the Moon and the Sun. For numerical integration, several integrators are available such as Runge-Kutta schemes of various orders.

4.4.2 Orbit determination

The orbit determination is performed independently for each fragment. The method used is a batch least squares estimation, which finds the initial Cartesian state vector of the fragment that minimizes the weighted sum of residuals between the observed and predicted angular positions over the entire observation arc.

The observations used as input are the right ascension and declination measurements from the previous section 4.3. Accounting for the imprecision of the WCS solution and of the fragment detection, a 1-sigma measurement noise of 2 arcseconds was considered on both right ascension and declination.

Since no independent initial orbit is known for the fragments, the initial state used to seed the estimator is propagated from LUCH's TLE at the epoch of the first observation using SGP4. To verify that this choice of initial guess does not introduce any bias in the final solution, the estimation was repeated several times with random perturbations added to the initial state. The fact that all runs converged to the same orbit solution confirms that the estimator is not sensitive to the initial guess in this context, and that the use of the parent TLE as a seed does not affect the final result.

The dynamical model used during the estimation includes an 8x8 spherical harmonic gravity field for the Earth, and point mass third body perturbations from the Sun and the Moon. Solar radiation pressure is not included in the force model, as the area-to-mass ratio of the fragments is unknown at this stage.

The evolution of the residuals over the iterations of the solving for fragment 3 is shown in Figure 4.6. The estimator converges in 3 iterations, which was also the case for all the other fragments. The orbits in state vectors are summarized in Table 4.4. The quality of the solutions found is assessed in section 4.4.3.

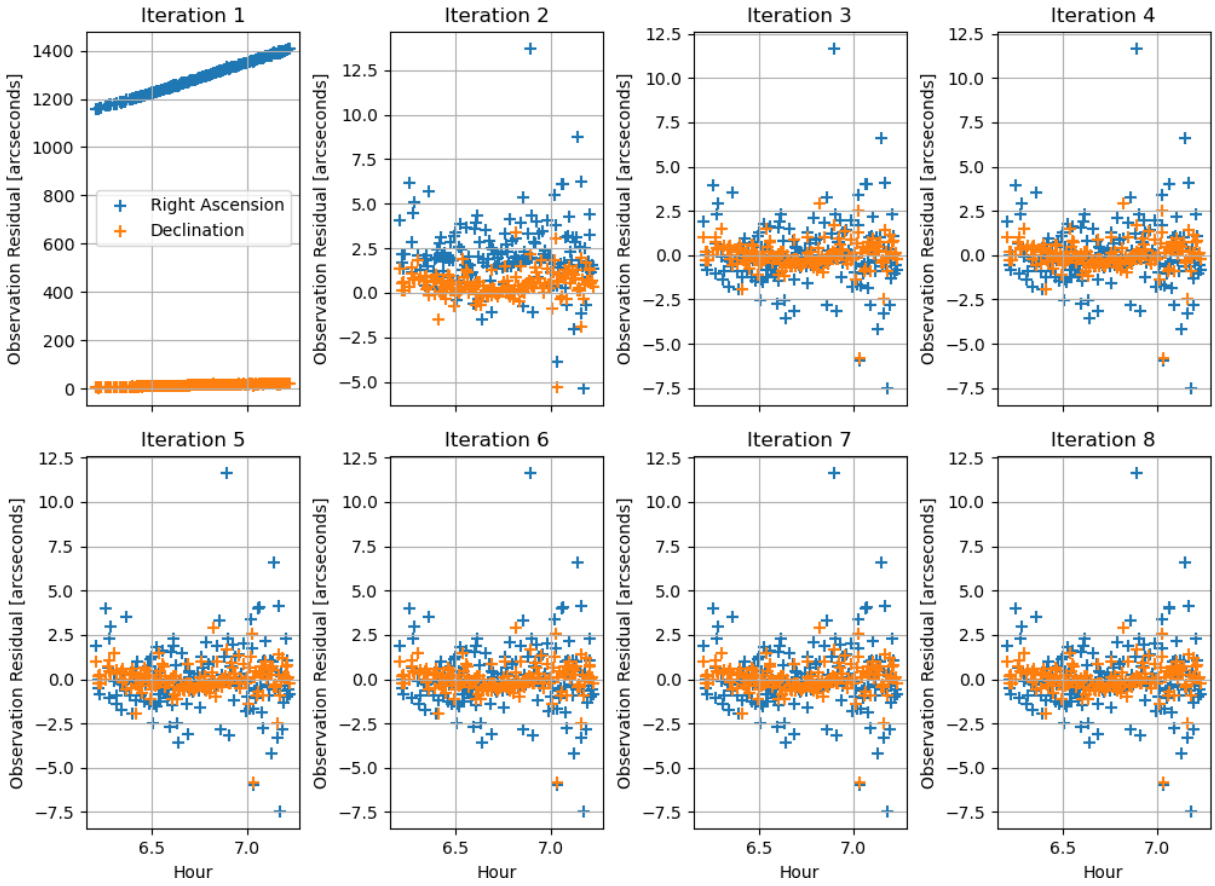

Figure 4.6: *Residuals evolution for fragment 3*

Fragment	x [km]	y [km]	z [km]	vx [m/s]	vy [m/s]	vz [m/s]
1	-39868.9	-14742.0	1130.8	1052.2	-2848.6	-43.4
2	-39480.8	-15686.1	1125.5	1150.3	-2848.0	-25.8
3	-39932.1	-14616.5	1135.9	1066.6	-2886.5	-37.8
4	-39594.2	-15477.5	1119.2	1140.8	-2854.0	-49.6
5	-38919.1	-16909.8	1093.5	1212.4	-2812.5	-39.4
6	-38447.7	-17910.5	1073.9	1287.3	-2773.4	-43.4
7	-28449.6	-31250.7	711.0	2253.6	-2054.4	-74.9
8	-32541.9	-27238.1	884.2	1962.8	-2348.6	-62.1
9	-34310.4	-24704.6	902.9	1791.9	-2486.6	-63.8

Table 4.4: *State vectors of determined orbits*

4.4.3 Quality of the orbits

Although an orbit solution was obtained for every fragment, the quality of the estimation varies significantly from one fragment to another, as reflected by the formal uncertainties derived from the covariance matrix of the least squares estimator, shown in Table 4.5. The orbit of fragment 5 is very well defined, while orbits of fragments 4, 6, 7 and 9 have a larger uncertainty.

Fragment	σ_x [km]	σ_y [km]	σ_z [km]	σ_{vx} [m/s]	σ_{vy} [m/s]	σ_{vz} [m/s]
1	247.1	122.6	30.6	14.7	14.8	0.8
2	189.5	99.8	23.7	12.1	11.1	0.5
3	29.7	14.6	3.6	2.2	1.5	0.1
4	341.9	177.6	42.7	20.8	20.8	1.1
5	5.5	3.2	0.7	0.5	0.2	0.0
6	300.8	181.4	38.6	20.3	17.5	1.0
7	374.3	511.4	64.0	44.4	17.9	2.0
8	50.8	52.7	7.6	5.4	2.0	0.2
9	426.2	382.1	60.6	36.6	23.5	1.7

Table 4.5: *Formal uncertainties for each orbits*

In order to validate the pipeline and the orbits found, it was necessary to have a point of comparison. Other organizations also observed the consequences of this event and produced some TLEs of the fragments they detected. To compare these orbits to the ones calculated in this work, the Mahalanobis distance was used [17, 18]. This tool enables to compare two orbits and quantitatively measure how different they are. The Mahalanobis distance compares two sets of orbital elements by scaling their geometric difference based on their combined covariance matrix, thereby effectively quantifying the distance between the two orbits in units of standard deviation. The lower the distance, the closer the orbits are. Figure 4.7 show a matrix of these distances. Fragment 2 is very close to debris with NORAD ID 91365, but the others cannot be confidently identified.

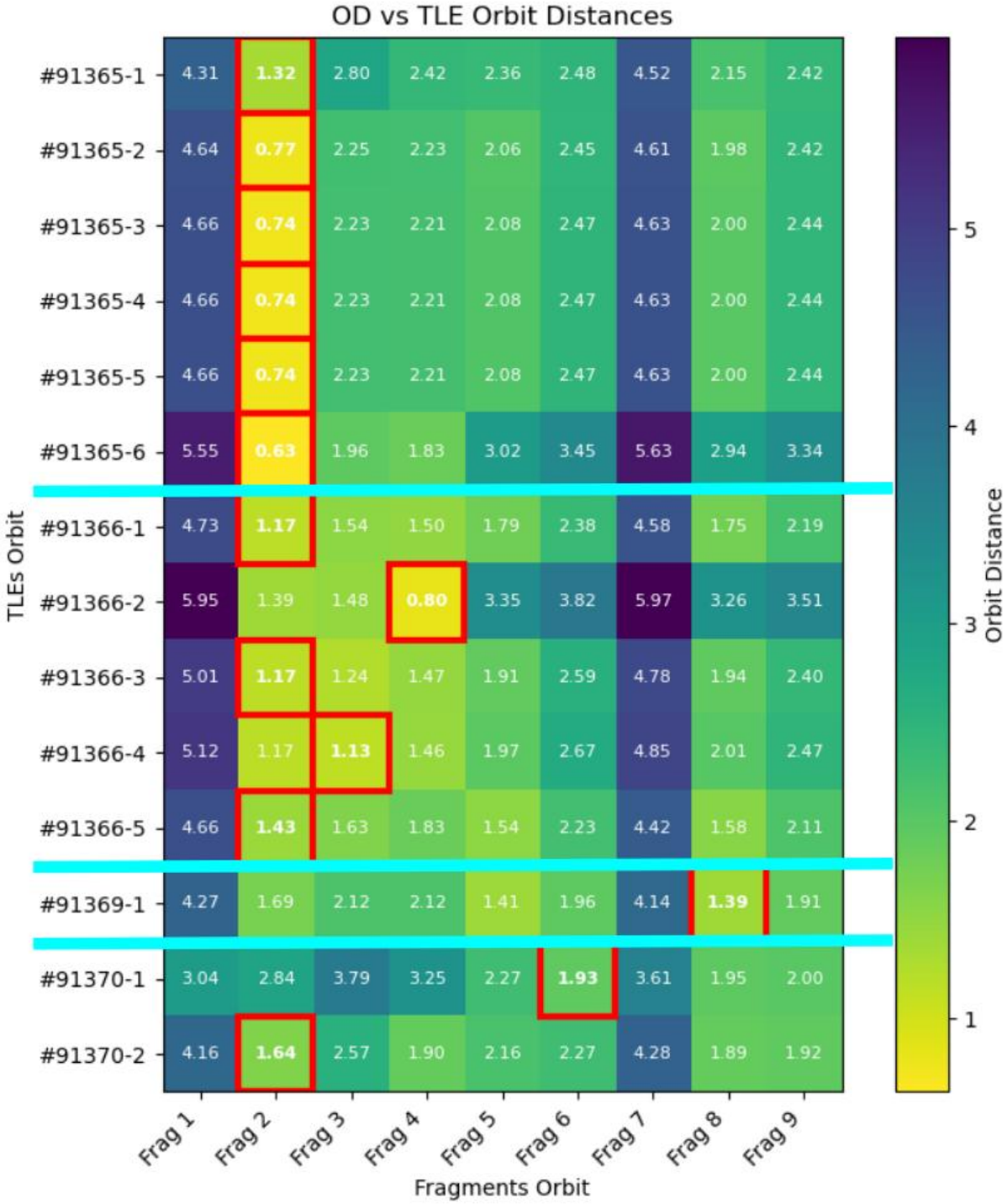

Figure 4.7: *Orbits distances matrix. TLEs are sorted by their NORAD IDs.*

5 Analysis

This section presents an analysis of the results using two tool, the Gabbard diagram and the NASA Standard Breakup Model (SBM).

5.1 Gabbard diagrams

The theoretical background of Gabbard diagrams can be found in section 2.6. Figure 5.1 shows the plot for the nine observed fragments. The fragments are approximately evenly distributed around the parent satellite, and the spread is low with orbital periods ranging from 1410 to 1480 minutes (roughly -40 to +25 minutes from parent satellite). An even distribution is generally explained by an explosion rather than a collision, which would introduce a bias toward one side of the plot.

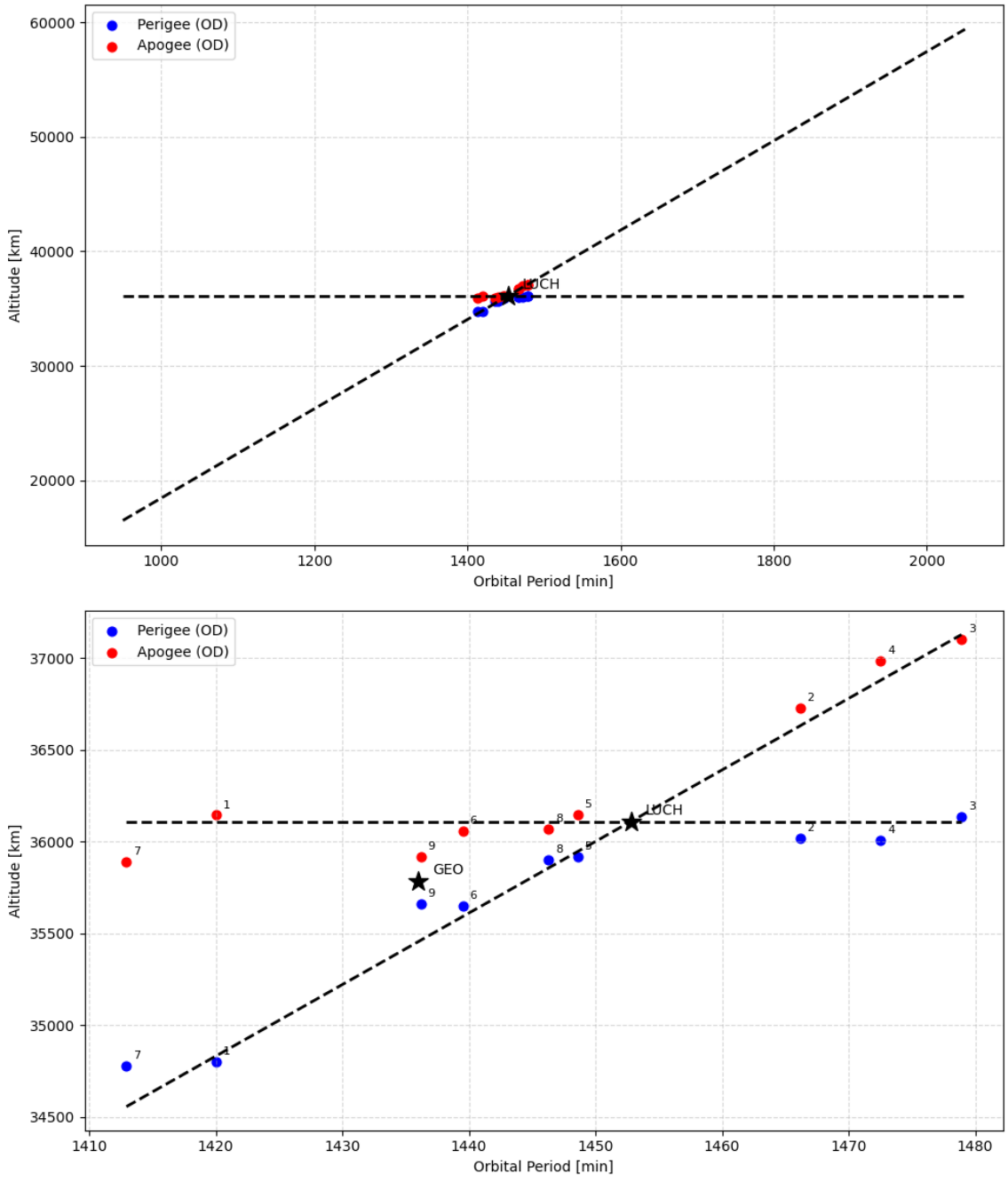

Figure 5.1: *Gabbard diagram for observed fragments*

We can see that some fragments are crossing the GEO region because of there elliptical orbit. Further study on the objects' orbit propagation has to be done to assess the risk of collision with another object happening.

5.2 SBM application to Luch/Olymp

The theoretical background of the SBM can be found in section 2.7. The implementation by ESA and TUM was used [19]. The input parameters are an explosion of a satellite with a mass of 2400kg (see 3.1). The model predicts 9264 objects between 1 and 10 cm, 235 objects between 10 cm and 1 m, and 10 objects larger than 1m. The median Δv is 58.48 m/s. The Gabbard diagram of all the debris larger than 10 cm is shown in Figure 5.2. The spread in orbital period is much higher than for the observed fragments, ranging around $\pm$ 300 minutes from the period of the parent object.

We can expect a higher orbital period spread is due to a higher range of Δv given to the debris during the explosion, which implies a higher explosion energy. The NASA SBM being tuned on rocket bodies fragmentation in LEO, this difference between observed and modeled debris population can be explained by multiple factors like the difference of explosion (batteries, tank overpressure...), the mass of the parent body or its geometry.

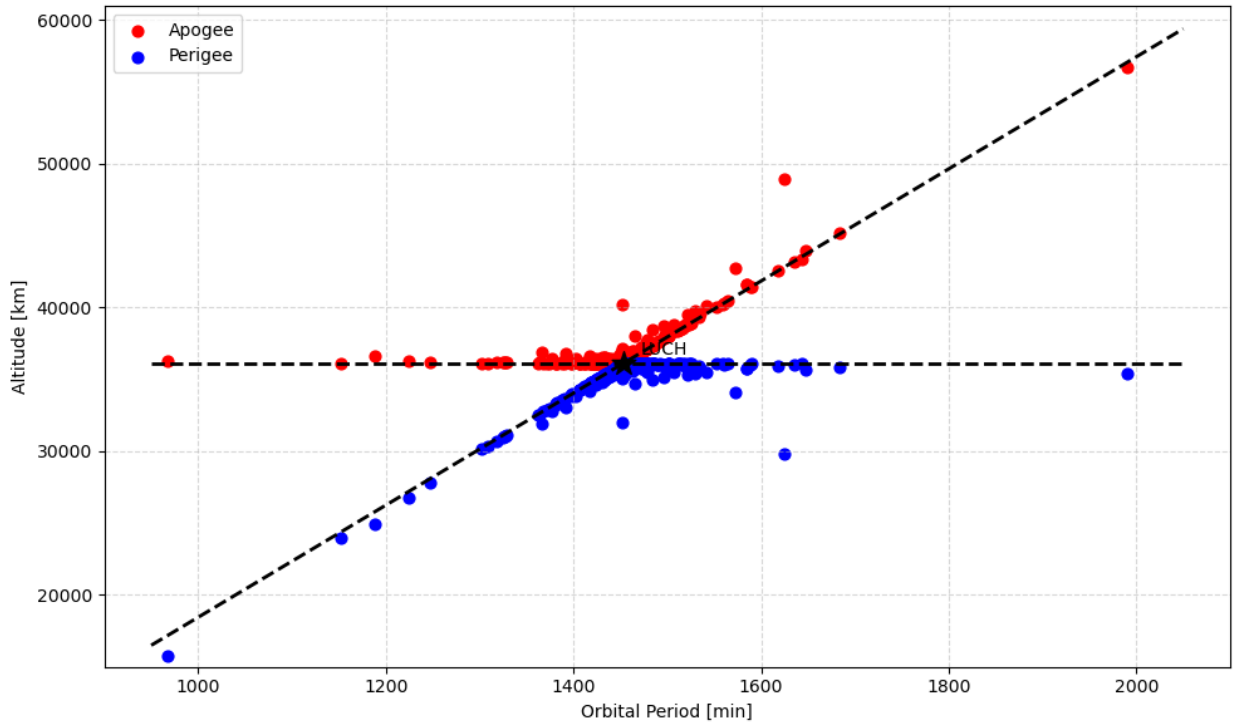

Figure 5.2: *Gabbard diagram of modeled fragments with no changes in parameters*

To account for these differences, the model was tuned, especially the parameter changing the Δv of the debris, named b. It is initially set to 1.85 in the SBM, and was changed from 1.0 to 2.0 in increments of 0.1. A KS test was then run between the 9 observed fragments and the population obtained with the model. The results are shown in Table 5.1. There seems to be a minimum in distance d at $b = 1.6$. This supports the hypothesis that the explosion of Luch has a lower energy than the explosions used to calibrate the SBM. However, with only 9 fragments in the observed population, this study would need more observations to have a robust test result.

b values	KS P values	KS d values
1.0	0.174	0.350
1.1	0.302	0.308
1.2	0.436	0.276
1.3	0.605	0.242
1.4	0.833	0.197
1.5	0.947	0.166
1.6	0.950	0.165
1.7	0.853	0.193
1.8	0.642	0.235
1.9	0.490	0.264
2.0	0.334	0.299

Table 5.1: *KS test for different b values*

Figure 5.3 shows the Gabbard diagram of only the 9 largest objects produced by the SBM with $b = 1.6$. It is very similar to the observed one, although the spread is a bit lower for the simulated diagram.

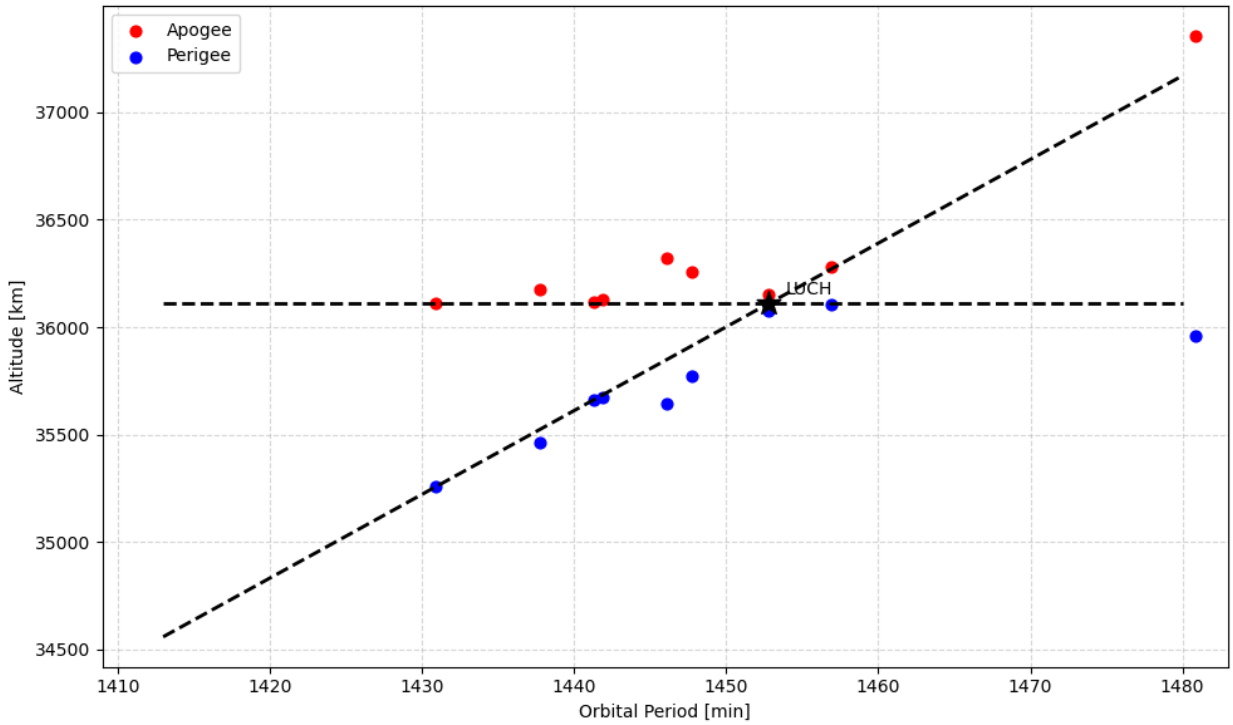

Figure 5.3: *Gabbard diagram of the 9 largest modeled fragments*

6 Discussion

This section describes the new breakup cause hypotheses, followed by a comparison with other GEO fragmentation event, and eventually the limitations of this project.

6.1 Breakup cause hypotheses revisited

The main hypotheses formulated shortly after the breakup were a passivation failure of the propulsion system or the batteries, either voluntary or involuntary, a hypervelocity impact from another object, or a deliberate destruction. It is not possible to determine the cause with certainty given the limitations of this study (see Section 6.3), but the available evidence allows one hypothesis to be prioritized over the others.

The fact that the event consisted of multiple successive explosions spread over more than half an hour, releasing fragments and gases, makes a hypervelocity impact unlikely. An impact would typically produce a single catastrophic fragmentation rather than a sequence of distinct events. A voluntary destruction cannot be entirely ruled out but is considered unlikely, as the geostationary region is a highly regulated and economically valuable environment where deliberate fragmentation would have serious consequences.

The satellite was not properly passivated before decommissioning, as evidenced by the fact that it maintained a stable attitude until the moment of the breakup, suggesting that residual stored energy was still present on board. A failure of an energetic subsystem is therefore the most probable cause. Between a propulsion system failure, such as a tank rupture, and a battery failure, the observed sequence of low energy events is more consistent with the latter. A cascading thermal runaway in the battery pack, where one or more degraded cells vented gas and the heat and debris from each event progressively triggered neighboring cells to fail in turn, would produce exactly this kind of sequential fragmentation spread over approximately half an hour, rather than the single high energy rupture expected from a propulsion failure.

6.2 Comparison with other GEO fragmentation events

Fragmentations in GEO are relatively rare and difficult to observe and characterize due to the distance. The *History of On-orbit Satellite Fragmentations* from NASA [20] and *DISCOSweb* from ESA [21] list all the breakup events that happened in orbit since the beginning of the space age. The list of all confirmed event in the GEO region is shown in Table 6.1. The only event similar to Luch/Olymp for which we have significant information to do a meaningful comparison is the fragmentation of Intelsat 33e.

Satellite / Object	International Designator	Breakup Date	Catalogued Fragments	Cause
Ekran 2	1977-092A	25 Jun 1978	4	Unknown
Titan 3C Transtage 5	1968-081E	21 Feb 1992	28	Unknown
Titan 3C Transtage 17	1969-013E	04 Jun 2014	0	Unknown
Briz-M upper stage	2015-075B	16 Jan 2016	6	Propulsion
Intelsat 33e	2016-053A	19 Oct 2024	36	Uncertain

Table 6.1: *Confirmed fragmentation events in the GEO region*

On October 19, 2024, the geostationary satellite Intelsat 33E suffered a sudden power failure and broke apart. The cause remains unconfirmed. Intelsat declared it a total loss within days. Tracked debris estimates grew rapidly and inconsistently, from an initial ≈20 pieces to ≈500 within a week [22].

The Gabbard diagram of the 36 publicly catalogued fragments is shown in Figure 6.1. The population has a small range of orbital period, similar to Luch, however the exact cause of the Intelsat 33e being unknown, it isn't possible to draw any conclusion that could help our analysis.

Modeling using the NASA SBM [23] estimated the generation of 4,393 fragments larger than 1 cm. Simulations showed the formation of high-density ring structures in the equatorial plane from 24 hours to 28 days after the breakup, and collision-risk assessments found that the top 10% of GEO satellites face a collision probability of up to 10^{-8} after 28 days, with satellites near the equatorial plane at higher risk than those in more inclined orbits. The debris population being similar between Luch and Intelsat 33e, these results should be similar, although a thorougher analysis with the exact orbits of Luch must be perform to get exact values.

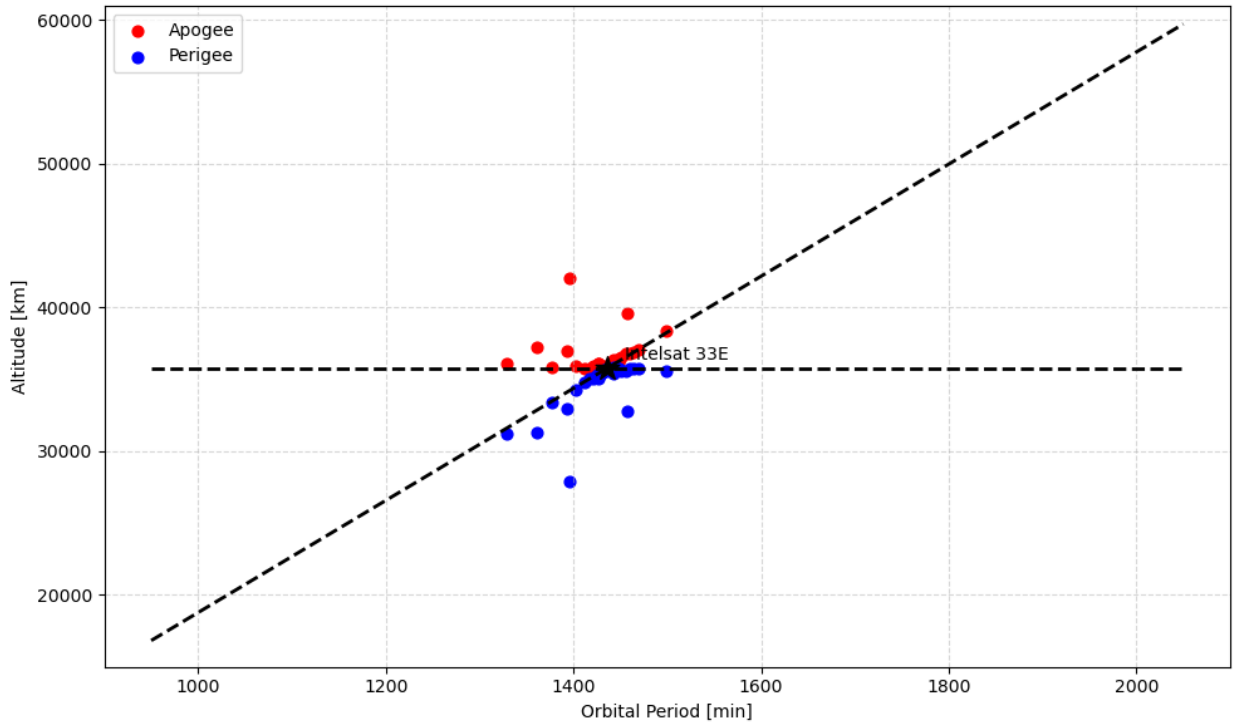

Figure 6.1: *Gabbard diagram of Intelsat33E fragments*

6.3 Limitations of the study

Several limitations were encountered during this project. The main one is the limited number of fragments that were successfully detected and for which an orbit has been determined. Even for those, the quality of the orbit is uncertain, with no ground truth comparison for 8 out of the 9. Some of the orbits have a huge uncertainty due to the short observation arc of only a few minutes for the worst ones. All these factors make the analysis weak as a fragmentation like this would likely produce hundreds or even thousands of objects, so the population analyzed is very small.

Another limitation is the usage of the NASA SBM in this context. This model was designed with data from upper stage explosions in LEO, and has its own assumptions like the fragments following a power-law distribution and the ejection being isotropic. This might not completely transfer to our case of study.

7 Conclusion

7.1 Summary of Achievements

This project successfully achieved its objectives of improving the knowledge on the Luch/Olymp fragmentation using the data collected by s2aSystems. An astrometric solution has been found for a majority of the dataset and several fragments were detected and tracked. This allowed the orbit determination for nine objects.

Based on these results, the event was analysed and discussed more in depth using diverse tools like Gabbard diagrams and the NASA Standard Breakup Model. It was determined that the cause of the breakup is probably a battery explosion. A comparison with another fragmentation event in GEO, the Intelsat 33e breakup, was made, and some limitations to this project were listed, mainly the small amount of detected fragments.

7.2 Future work

Several action point can be taken to improve the overall results. Firstly, this study didn't use the long exposure images. These contain a lot more information that could be used to detect new fragments and improve those already detected. Other techniques could also be applied like synthetic tracking, to enhance the visibility of faint fragments and detect new ones in the dataset used in this project. On a later stage of using these data, long-term orbit propagation can be performed to assess the threat of the resulting debris cloud to operational geostationary satellites. Finally, improvement of the NASA SBM to get better results for small energy event, and more accurate values for very small debris could be investigated.

7.3 Lessons learned

Througout this project, I learned a lot about the SSA domain and how astronomical images are processed. I discovered many new tools like Astropy or Astrometry.net. A significant amount of time was spent on the orbit determination pipeline. Getting Tudat to produce consistent results was more difficult than initially expected, and a large part of the difficulty came from reference frame issues. Ensuring that the observations, the initial state from the TLE, and the dynamical model were all expressed in the same frame required careful attention, and several apparently correct implementations turned out to produce wrong results due to subtle frame conversion errors.

On a broader level, this project gave me a much more concrete understanding of the space debris problem. Before starting, the topic was mostly abstract. Working directly with observations of a real fragmentation event, processing the data, and seeing the fragment cloud in the results made the stakes of the problem much more tangible. I now have a clearer sense of both the technical complexity of monitoring the debris environment and the importance of the work done by SSA operators on a daily basis.

References

[1] "Esa's annual space environment report," Tech. Rep. 10, ESA Space Debris Office, May 2026.

[2] E. Johnston, "List of satellites in geostationary orbit." Retrieved June 11, 2026, from `https://www.satsig.net/sslist.htm`.

[3] M. Capderou, *Handbook of Satellite Orbits, From Kepler to GPS*, ch. 6. Springer, 2014.

[4] D. J. Kessler and B. G. Cour-Palais, "Collision frequency of artificial satellites: The creation of a debris belt," *Journal of Geophysical Research: Space Physics*, vol. 83, no. A6, pp. 2637–2646, 1978.

[5] T. Kelso, "Analysis of the iridium 33 - cosmos 2251 collision," *Proceedings of the 19th AIAA/AAS Astrodynamics Specialist Conference*, vol. 135, 09 2009.

[6] N. L. Johnson, E. Stansbery, J.-C. Liou, M. Horstman, C. Stokely, and D. Whitlock, "The characteristics and consequences of the break-up of the fengyun-1c spacecraft," *Acta Astronautica*, vol. 63, no. 1, pp. 128–135, 2008.

[7] A. Tan, R. C. Reynolds, and M. Schamschula, "Noaa-16 satellite fragmentation in orbit: Genesis of the gabbard diagram and estimation of the intensity of breakup," *Advances in Aerospace Science and Applications*, vol. 7, no. 1, pp. 37–47, 2017.

[8] N. Johnson, P. Krisko, J.-C. Liou, and P. Anz-Meador, "Nasa's new breakup model of evolve 4.0," *Advances in Space Research*, vol. 28, no. 9, pp. 1377–1384, 2001.

[9] J. C. McDowell, "Gcat: General catalog of artificial space objects." Retrieved June 16, 2026, from `https://planet4589.org/space/gcat/web/cat/index.html`.

[10] D. Krebs Gunter, "Luch-kh/olimp-k." Retrieved June 16, 2026, from `https://space.skyrocket.de/doc_sdat/olimp-k.htm`.

[11] Astropy Collaboration, T. P. Robitaille, E. J. Tollerud, P. Greenfield, M. Droettboom, E. Bray, T. Aldcroft, M. Davis, A. Ginsburg, A. M. Price-Whelan, W. E. Kerzendorf, A. Conley, N. Crighton, K. Barbary, D. Muna, H. Ferguson, F. Grollier, M. M. Parikh, P. H. Nair, H. M. Unther, C. Deil, J. Woillez, S. Conseil, R. Kramer, J. E. H. Turner, L. Singer, R. Fox, B. A. Weaver, V. Zabalza, Z. I. Edwards, K. Azalee Bostroem, D. J. Burke, A. R. Casey, S. M. Crawford, N. Dencheva, J. Ely, T. Jenness, K. Labrie, P. L. Lim, F. Pierfederici, A. Pontzen, A. Ptak, B. Refsdal, M. Servillat, and O. Streicher, "Astropy: A community Python package for astronomy," *Astronomy & Astrophysics*, vol. 558, p. A33, Oct. 2013.

[12] Astropy Collaboration, A. M. Price-Whelan, B. M. Sipőcz, H. M. Günther, P. L. Lim, S. M. Crawford, S. Conseil, D. L. Shupe, M. W. Craig, N. Dencheva, A. Ginsburg, J. T. Vand erPlas, L. D. Bradley, D. Pérez-Suárez, M. de Val-Borro, T. L. Aldcroft, K. L. Cruz, T. P. Robitaille, E. J. Tollerud, C. Ardelean, T. Babej, Y. P. Bach, M. Bachetti, A. V. Bakanov, S. P. Bamford, G. Barentsen, P. Barmby, A. Baumbach, K. L. Berry, F. Biscani, M. Boquien, K. A. Bostroem, L. G. Bouma, G. B. Brammer, E. M. Bray, H. Breytenbach, H. Buddelmeijer, D. J. Burke, G. Calderone, J. L. Cano Rodríguez, M. Cara, J. V. M. Cardoso, S. Cheedella, Y. Copin, L. Corrales, D. Crichton, D. D'Avella, C. Deil, É. Depagne, J. P. Dietrich, A. Donath, M. Droettboom, N. Earl, T. Erben, S. Fabbro, L. A. Ferreira, T. Finethy, R. T. Fox, L. H. Garrison, S. L. J. Gibbons, D. A. Goldstein, R. Gommers, J. P. Greco, P. Greenfield, A. M. Groener, F. Grollier, A. Hagen, P. Hirst, D. Homeier, A. J. Horton, G. Hosseinzadeh, L. Hu, J. S. Hunkeler, Ž. Ivezić, A. Jain, T. Jenness, G. Kanarek, S. Kendrew, N. S. Kern, W. E. Kerzendorf, A. Khvalko, J. King, D. Kirkby, A. M. Kulkarni, A. Kumar, A. Lee, D. Lenz, S. P. Littlefair, Z. Ma, D. M. Macleod, M. Mastropietro, C. McCully, S. Montagnac, B. M. Morris, M. Mueller, S. J. Mumford, D. Muna, N. A. Murphy, S. Nelson, G. H. Nguyen, J. P. Ninan, M. Nöthe, S. Ogaz, S. Oh, J. K. Parejko, N. Parley, S. Pascual, R. Patil, A. A. Patil, A. L. Plunkett, J. X. Prochaska, T. Rastogi, V. Reddy Janga, J. Sabater, P. Sakurikar, M. Seifert,

L. E. Sherbert, H. Sherwood-Taylor, A. Y. Shih, J. Sick, M. T. Silbiger, S. Singanamalla, L. P. Singer, P. H. Sladen, K. A. Sooley, S. Sornarajah, O. Streicher, P. Teuben, S. W. Thomas, G. R. Tremblay, J. E. H. Turner, V. Terrón, M. H. van Kerkwijk, A. de la Vega, L. L. Watkins, B. A. Weaver, J. B. Whitmore, J. Woillez, V. Zabalza, and Astropy Contributors, "The Astropy Project: Building an Open-science Project and Status of the v2.0 Core Package," *The Astronomical Journal*, vol. 156, p. 123, Sept. 2018.

[13] Astropy Collaboration, A. M. Price-Whelan, P. L. Lim, N. Earl, N. Starkman, L. Bradley, D. L. Shupe, A. A. Patil, L. Corrales, C. E. Brasseur, M. N"othe, A. Donath, E. Tollerud, B. M. Morris, A. Ginsburg, E. Vaher, B. A. Weaver, J. Tocknell, W. Jamieson, M. H. van Kerkwijk, T. P. Robitaille, B. Merry, M. Bachetti, H. M. G"unther, T. L. Aldcroft, J. A. Alvarado-Montes, A. M. Archibald, A. B'odi, S. Bapat, G. Barentsen, J. Baz'an, M. Biswas, M. Boquien, D. J. Burke, D. Cara, M. Cara, K. E. Conroy, S. Conseil, M. W. Craig, R. M. Cross, K. L. Cruz, F. D'Eugenio, N. Dencheva, H. A. R. Devillepoix, J. P. Dietrich, A. D. Eigenbrot, T. Erben, L. Ferreira, D. Foreman-Mackey, R. Fox, N. Freij, S. Garg, R. Geda, L. Glattly, Y. Gondhalekar, K. D. Gordon, D. Grant, P. Greenfield, A. M. Groener, S. Guest, S. Gurovich, R. Handberg, A. Hart, Z. Hatfield-Dodds, D. Homeier, G. Hosseinzadeh, T. Jenness, C. K. Jones, P. Joseph, J. B. Kalmbach, E. Karamehmetoglu, M. Kaluszy'nski, M. S. P. Kelley, N. Kern, W. E. Kerzendorf, E. W. Koch, S. Kulumani, A. Lee, C. Ly, Z. Ma, C. MacBride, J. M. Maljaars, D. Muna, N. A. Murphy, H. Norman, R. O'Steen, K. A. Oman, C. Pacifici, S. Pascual, J. Pascual-Granado, R. R. Patil, G. I. Perren, T. E. Pickering, T. Rastogi, B. R. Roulston, D. F. Ryan, E. S. Rykoff, J. Sabater, P. Sakurikar, J. Salgado, A. Sanghi, N. Saunders, V. Savchenko, L. Schwardt, M. Seifert-Eckert, A. Y. Shih, A. S. Jain, G. Shukla, J. Sick, C. Simpson, S. Singanamalla, L. P. Singer, J. Singhal, M. Sinha, B. M. SipHocz, L. R. Spitler, D. Stansby, O. Streicher, J. Sumak, J. D. Swinbank, D. S. Taranu, N. Tewary, G. R. Tremblay, M. d. Val-Borro, S. J. Van Kooten, Z. Vasovi'c, S. Verma, J. V. de Miranda Cardoso, P. K. G. Williams, T. J. Wilson, B. Winkel, W. M. Wood-Vasey, R. Xue, P. Yoachim, C. Zhang, A. Zonca, and Astropy Project Contributors, "The Astropy Project: Sustaining and Growing a Community-oriented Open-source Project and the Latest Major Release (v5.0) of the Core Package," *The Astrophysical Journal*, vol. 935, p. 167, Aug. 2022.

[14] L. Bradley, B. M. Sipőcz, T. P. Robitaille, E. J. Tollerud, Z. Vinícius, C. Deil, K. Barbary, T. J. Wilson, I. Busko, A. Donath, H. M. Günther, M. Cara, P. L. Lim, S. Meßlinger, S. Conseil, M. Droettboom, K. A. Bostroem, E. M. Bray, L. A. Bratholm, Z. Burnett, W. Jamieson, A. Ginsburg, D. Taranu, G. Barentsen, M. W. Craig, B. M. Morris, M. Perrin, and S. Rathi, "Photutils," Apr. 2026.

[15] D. Lang, D. W. Hogg, K. Mierle, M. Blanton, and S. Roweis, "Astrometry.net: Blind Astrometric Calibration of Arbitrary Astronomical Images," *The Astronomical Journal*, vol. 139, pp. 1782–1800, May 2010.

[16] L. Gisolfi, D. Dirkx, S. Fayolle, V. Filice, R. Alkahal, M. Avillez, T. Dijkstra, J. Hener, L. Hinüber, M. Langbroek, N. Maistri, M. Plumaris, A. S. Rodriguez, G. Cimò, K. Cowan, F. Dahmani, J. Encarnacao, G. Garrett, S. Gehly, X. Hu, M. Jeanjean, A. L. Rivera, A. M. Amodio, G. M. Calvés, M. Reichel, B. Root, M. Søndergaard, D. Stiller, S. V. Hulle, G. V. Kleijn, R. Williams, and D. Witte, "Open-source high-fidelity orbit estimation for planetary science and space situational awareness using the tudat software," 2025.

[17] A. Vananti, M. M. zu Westram, and T. Schildknecht, "Metrics on space of closed orbits for near-earth objects identification," *Celestial Mechanics and Dynamical Astronomy*, 2023.

[18] K. V. Kholshevnikov, G. I. Kokhirova, P. B. Babadzhanov, and U. H. Khamroev, "Metrics in the space of orbits and their application to searching for celestial objects of common origin," *Monthly Notices of the Royal Astronomical Society*, vol. 462, no. 2, pp. 2275–2283, 2016.

[19] J. Schuhmacher, "Efficient implementation and evaluation of the nasa breakup model in modern

c++," Master's thesis, Technical University of Munich, Sep 2021.

[20] P. Anz-Meador, J. N. Opiela, D. Shoots, and J.-C. Liou, "History of on-orbit satellite fragmentations, 16th edition," Tech. Rep. NASA/TP-20220019160, NASA Johnson Space Center, Orbital Debris Program Office, December 2022.

[21] European Space Agency, "DISCOSweb Database." https://discosweb.esoc.esa.int/. Retrieved July 3, 2026.

[22] J. Rainbow, "Exoanalytic observes 500 pieces of debris from intelsat 33e breakup." Retrieved July 6, 2026, from https://spacenews.com/exoanalytic-observes-500-pieces-of-debris-from-intelsat-33e-breakup/.

[23] P. Shu, M. Zhao, Y. Wu, and et al., "Distribution and evolution of the debris cloud from the fragmentation of intelsat 33e," vol. 13, no. 4, p. 303, 2026.